Front. Earth Sci. 2024, 18(4): 683–695
https://doi.org/10.1007/s11707-024-1133-y

RESEARCH ARTICLE

Further geochronological constraints on the Xiuyan impact crater in northeast China

Zeyang ZHU[1], Chang HUANG (✉)[2], Jing WU[1], Yawei LI[3], Zhihao SUN[1], Min ZHANG[4,5], Bin ZHANG[1], Sheng-Hua LI[2], Jiaqi LIU[1]

1 Key Laboratory of Cenozoic Geology Environment, Institute of Geology and Geophysics, Chinese Academy of Sciences, Beijing 100029, China
2 Department of Earth Sciences, The University of Hong Kong, Hong Kong 999077, China
3 College of Tourism and Planning, Pingdingshan University, Pingdingshan 467400, China
4 School of Water Conservancy and Transportation, Zhengzhou University, Zhengzhou 450000, China
5 Geothermal and Ecological Geology Research Center, Zhengzhou University, Zhengzhou 450000, China

Abstract The Xiuyan impact crater is the only officially recognized impact crater in China, and its formation time remains unclear. In this study, we investigated the ages of Xiuyan impact crater lake sediments from a 99-m composite borehole using luminescence and radiocarbon dating. The results showed that all the radiocarbon ages were saturated and that the surface sediments in the crater lake were dated to ~331–334 ka. Furthermore, the luminescence ages of lake sediments at depths below approximately 37 m also appear to be saturated. The evolutionary history of the Xiuyan impact crater lake was reconstructed by incorporating sedimentological, geomorphological, and geochronological analyses. Based on the age-depth model results of luminescence ages above a depth of 37 m, it is suggested that the crater lake underwent several stages: initial formation at approximately 1201 ± 133 ka, subsequent filling with water and sediment, overflow, and eventual disappearance at ~331–334 ka.

Keywords Xiuyan impact crater, luminescence dating, age saturation, impact age, northeast China

1 Introduction

Interplanetary body impacts are important geological processes in the Earth's history and provide essential information about other solar system bodies (Grieve and Pesonen, 1992). In addition, impact events have likely severely affected the terrestrial environment, such as with the Younger Dryas abrupt cooling event (Firestone et al., 2007, Sweatman, 2021), and even biological survival, such as with the well-known mass extinction at the Cretaceous–Paleogene boundary (Schulte et al., 2010). Accurately determining the chronology of these impact events enables us to understand the link between impact events and changes in the biosphere and climate. However, only a few impact events are well dated, especially impact events that have occurred during the Quaternary (Jourdan et al., 2012, Schmieder and Kring, 2020).

The Xiuyan impact crater, located in northeast China (Fig. 1), is the only officially recognized impact crater in China, according to the Earth Impact Database (available at Earth Impact Database website). Liu et al. (2013) reported an age of ~50 thousand years (ka) for crater formation using radiocarbon dating of lacustrine sediments. However, the relatively young upper age limit of < 50 ka and the deposition rate (~1 cm/year) of the lake sediments indicate that the reported ages of the Xiuyan impact event are probably underestimated and that other dating strategies should be used. For example, luminescence dating has been successfully employed to constrain the age of Quaternary sediments to approximately 500 ka (Jacobs et al., 2018) or even 780 ka (Rui et al., 2020). Therefore, in this study, both luminescence and radiocarbon dating methods were used to evaluate lake sediments in the Xiuyan impact crater to further constrain the age of the impact event and reconstruct the evolution of this impact crater lake.

2 Materials and methods

2.1 Study site

The Xiuyan crater (40°22′N, 123°28′E) is a bowl-shaped

Received February 2, 2024; accepted June 21, 2024

E-mail: chang92@connect.hku.hk

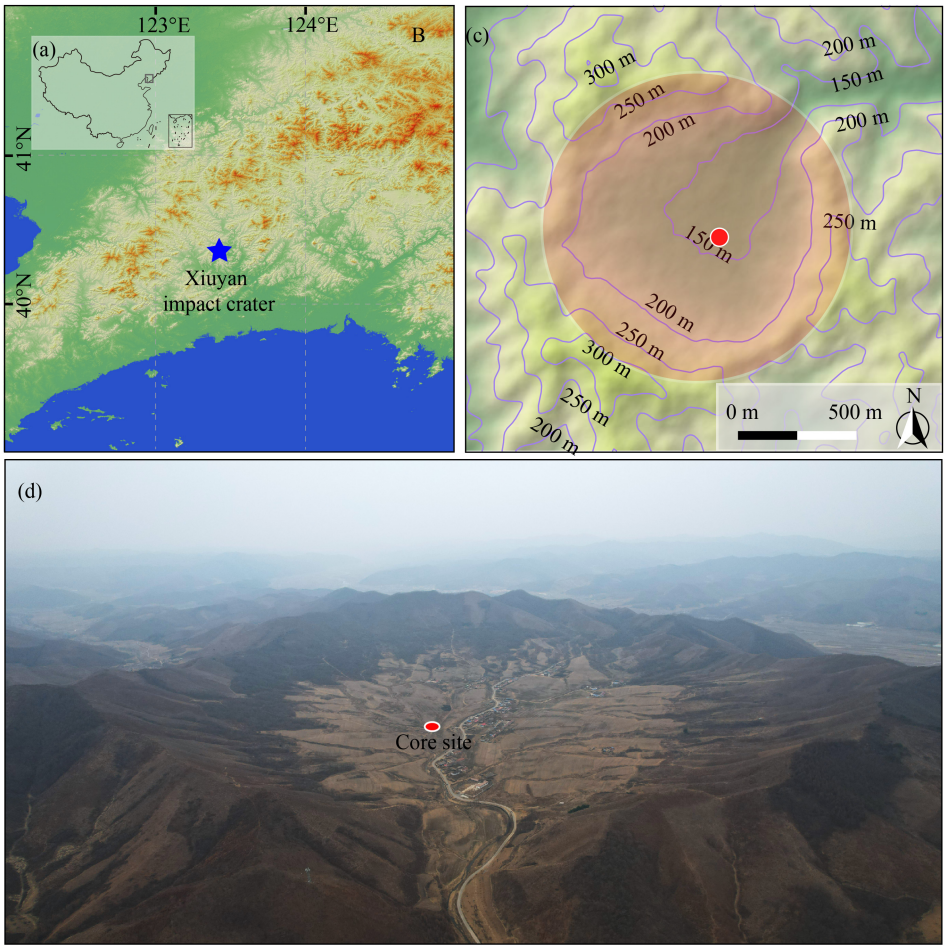

Fig. 1 (a) Location of the study area. (b) Location of the Xiuyan impact crater (blue star). (c) Topographic map of the Xiuyan impact crater and the coring location (red dot). (d) Photograph of the Xiuyan impact crater taken from a distance; the red dot is the coring site.

simple impact crater located in the Liaodong Peninsula in northeast China (Fig. 1). The nearly circular crater has a diameter of ~1.8 km and a depth of ~149 m from the impact crater rim to the crater bottom (Wang et al., 2013). The crater is characterized by a circular rim and has an outlet at its northeastern part. The highest part of the rim is located in the southwestern part of the crater and has an altitude of ~344 m above sea level, and the lowest point lies at the outlet and an altitude of ~120 m (Fig. 1(c)) (Wang et al., 2013). The crater is located in Proterozoic metamorphic rocks, i.e., granulite, hornblendite, gneiss, marble, and tremolite marble (Chen et al., 2009). The crater is filled with breccia consisting of granulite, hornblendite, gneiss, and tremolite marble at depths ranging from ~295 m to ~107 m beneath the ground. The breccia layer is overlain by ~107-m-thick Quaternary lake sediments (Fig. 2) (Chen et al., 2009). Currently, the crater is dry and is used for crop cultivation.

2.2 Borehole description and sampling

Two parallel cores with depths of 100.0 m (Xiuyan-A) and 103.8 m (Xiuyan-B) were recovered from the center of the Xiuyan crater in April 2020. The Xiuyan cores are predominantly composed of fine green grayish to dark silt and silty clays, occasionally intercalated with siderite layers, gravel layers, and peat (Fig. 2). Specifically, disordered silt laminations with white and dark thin sand layers occur in the deepest part of the core (~105–100 m). Above 100 m, a thick layer of fine green grayish to dark silt and silty clay is observed, with sporadic laminations between ~100 and ~23 m. Additionally, an ~3.4-m-thick peat layer (11.9–8.5 m) with abundant wood fragments and organic detritus is present. Subsequently, the sediments consist of steel gray and grayish-white sandy silt layers and gravel layers in the uppermost part of the core (Fig. 2).

Five residual plant samples (stems and leaves of terrestrial plants) for radiocarbon dating were collected from ~15.2 m to 7.0 m deep in the core (Fig. 2). A total of 24 luminescence samples were collected from the sediment core, ranging from the top (~1.7 m) to the bottom (~99.1 m) of core A. Each luminescence sample measuring 15 cm in length was obtained from the bottom section of the core. The samples were sealed in a black plastic tube and wrapped in aluminum foil to avoid moisture loss

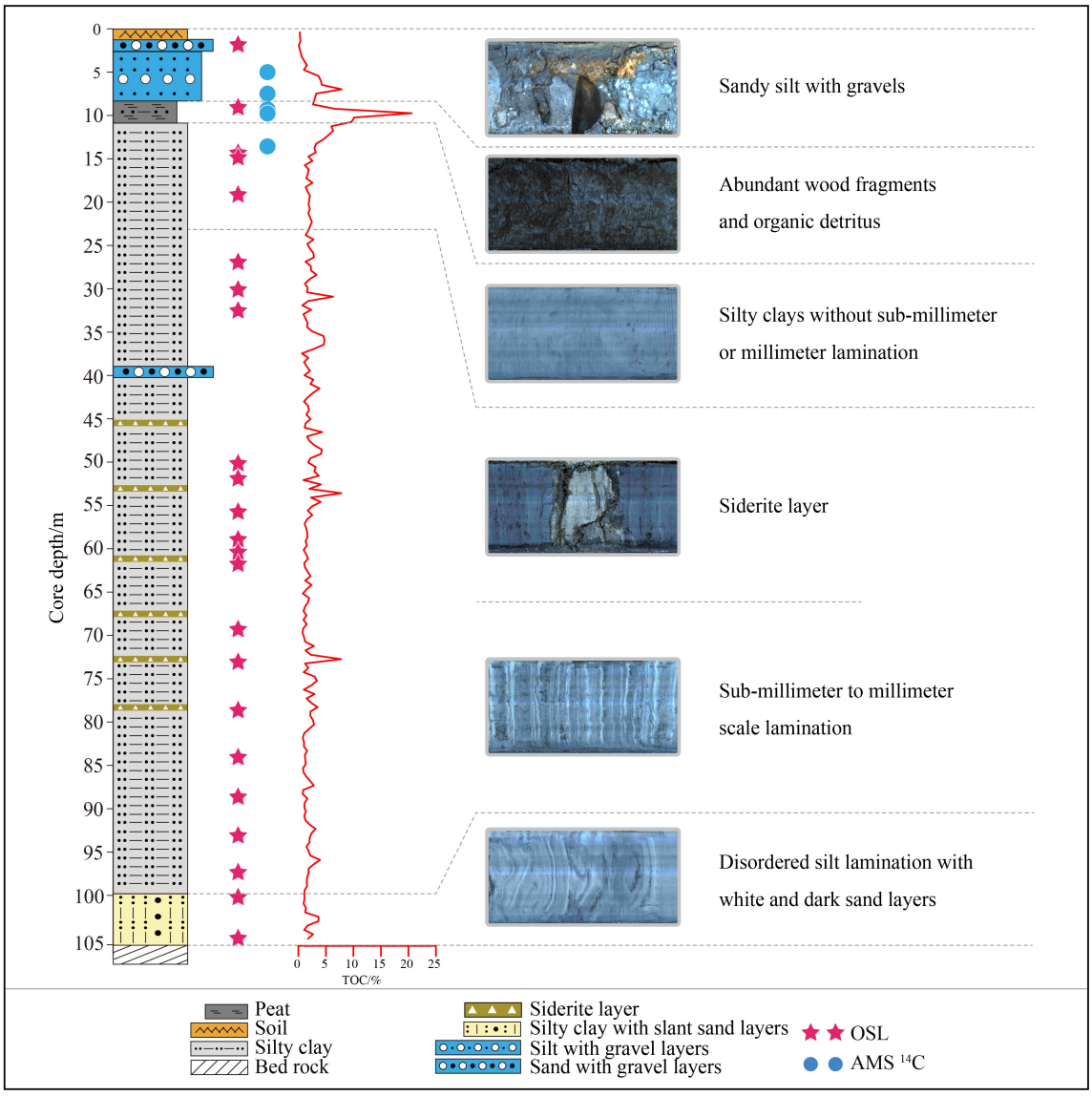

Fig. 2 Lithology, sampling information, total organic carbon (TOC), and representative lithological pictures of the core.

and light exposure.

2.3 Radiocarbon dating

The ^{14}C samples were pretreated and analyzed at the Beta Analytic Radiocarbon Dating Laboratory (Florida, USA) and converted into calendar years using the online OxCal V4.4.4 software (Ramsey, 2009) and the IntCal20 calibration curve (Reimer et al., 2020). The calibrated ^{14}C age in units of ka (the ^{14}C age represents the age before 1950 CE) was used for comparison with the luminescence ages.

2.4 Luminescence dating

2.4.1 Sample preparation and measurements

Sample preparation for luminescence dating was conducted under subdued red light in the laboratory following standard luminescence dating laboratory procedures at the University of Hong Kong, China. The outer 2–3 cm of deposits on the sample surface were removed and reserved for radioactive isotope (e.g., U, Th, and K) measurements. The remaining inner part of the sample was prepared for equivalent dose (D_e) determination. Then, 10% hydrochloric acid and 30% hydrogen peroxide solutions were used to remove the carbonates and organic matter, respectively. The coarse-grain fractions with diameters ranging from 63 to 90, 90–125, and 90–150 μm (depending on availability) were obtained by wet sieving. Potassium feldspar (K-feldspar) grains were then extracted using heavy liquids, with a density range of 2.52–2.58 g/cm^3. After drying, the K-feldspar grains were etched with 10% HF for ~10 min to remove the outer layer irradiated by alpha particles. The etched grains were then treated with 10% hydrochloric acid for ~10 min to

remove any acid-soluble fluoride precipitates. The etched K-feldspar grains were then mounted on 9.7-mm stainless steel discs (3–4 mm in diameter), with silicone oil as an adhesive.

Luminescence measurements were carried out on an automated Risø TL/OSL DA-15 Reader equipped with a $^{90}Sr/^{90}Y$ beta source (0.07 Gy/s on stainless steel discs) (Bøtter-Jensen et al. 2010). Infrared LEDs (875 ± 40 nm) were utilized for K-feldspar stimulation. Luminescence signals were detected by a photomultiplier tube through a filter pack comprising Schott BG-39 and Corning 7-59 filters. Additionally, the samples were bleached using a solar simulator (Hönle SOL2) with a 1000 W xenon arc lamp.

2.4.2 Standardized growth curve (SGC) method

Considering the potential older ages (e.g., > 50 ka) of the core sediments, the 'multiple aliquot regenerative-dose (MAR) with 'heat' protocol using multiple-elevated-temperature (MET) post infrared infrared (pIRIR) signals of K-feldspar was employed (Table 1) (Li and Li, 2011; Li et al., 2013; Chen et al., 2015; Zhang et al., 2021, 2022). In this protocol, all aliquots were preheated at 320°C for 60 s and then stimulated with IR light at 50°C, 100°C, 150°C, 200°C, 250°C, and 300°C for 100 s (Table 1). Before the test dose, all aliquots were heated to 500°C to eliminate the 'pre-dose memory', increasing the average D_0 value to ~750 Gy (Li et al., 2013; Chen et al., 2015; Zhang et al., 2022). The MET-pIRIR signals at higher temperatures (e.g., 250°C and 300°C) were likely free of anomalous fading; thus, no fading correction was required (Li and Li, 2011 and 2012). Figure 3 shows the IRSL and pIRIR decay curves for one aliquot of sample A01-A. The first 10 s of the decay curve of the IRSL and pIRIR signals were used for D_e calculations, with the last 10 s signal treated as background and subtracted.

A total of 11 samples collected from various depths of the sediment borehole were measured to establish a 'MAR SGC' curve using the 'MAR with heat' protocol, with the 'regenerative-dose normalization' method (Table1). The protocol for K-feldspar is based on the establishment of an SGC curve constructed from the renormalized L_x/T_x signals of multiple aliquot groups (Li et al., 2013; Li et al., 2017). The detailed steps are shown

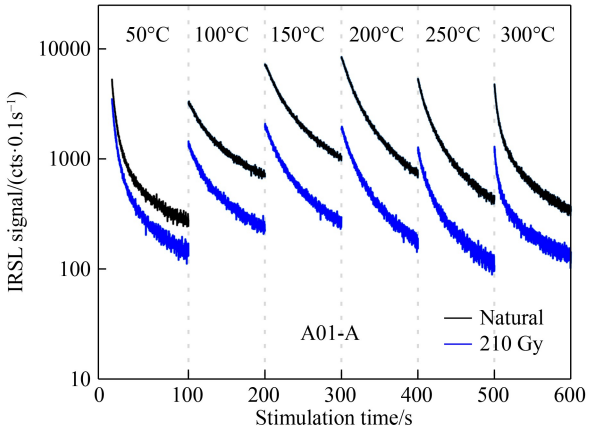

Fig. 3 Natural and test dose decay curves of K-feldspar IRSL and MET-pIRIR signals for an aliquot from sample A01-A.

Table 1 'MAR with heat' dating protocol using MET-pIRIR signals, modified from Li et al. (2013) and Chen et al. (2015).

Step	Treatment	Observed
1	Give regenerative dose, D_i	
2	Preheat at 320°C for 60 s	
3	Take IRSL measurement at 50°C for 100 s	$L_x(50)$
4	Take IRSL measurement at 100°C for 100 s	$L_x(100)$
5	Take IRSL measurement at 150°C for 100 s	$L_x(150)$
6	Take IRSL measurement at 200°C for 100 s	$L_x(200)$
7	Take IRSL measurement at 250°C for 100 s	$L_x(250)$
8	Take IRSL measurement at 300°C for 100 s	$L_x(300)$
9	Cutheat to 500°C	
10	Give test dose, D_t	
11	Preheat at 320°C for 60 s	
12	Take IRSL measurement at 50°C for 100 s	$T_x(50)$
13	Take IRSL measurement at 100°C for 100 s	$T_x(100)$
14	Take IRSL measurement at 150°C for 100 s	$T_x(150)$
15	Take IRSL measurement at 200°C for 100 s	$T_x(200)$
16	Take IRSL measurement at 250°C for 100 s	$T_x(250)$
17	Take IRSL measurement at 300°C for 100 s	$T_x(300)$

below.

1) The aliquots from 11 samples were bleached using a solar simulator for ~8 h.

2) These bleached aliquots were divided into several groups and given different regenerative doses ranging from 0 to 3000 Gy (Fig. 4). The test doses were fixed at 210 Gy. Among them, one group of aliquots for each sample was given a regenerative dose of ~600 Gy for 'regenerative-dose normalization'.

3) For each sample, the sensitivity-corrected luminescence signal (L_x/T_x) of all the aliquots was normalized to the mean L_x/T_x value of the aliquots dosed with 600 Gy. The test doses of all MAR measurements remained fixed at 210 Gy.

4) The renormalized L_x/T_x values of all aliquots were plotted against their corresponding regenerative doses and

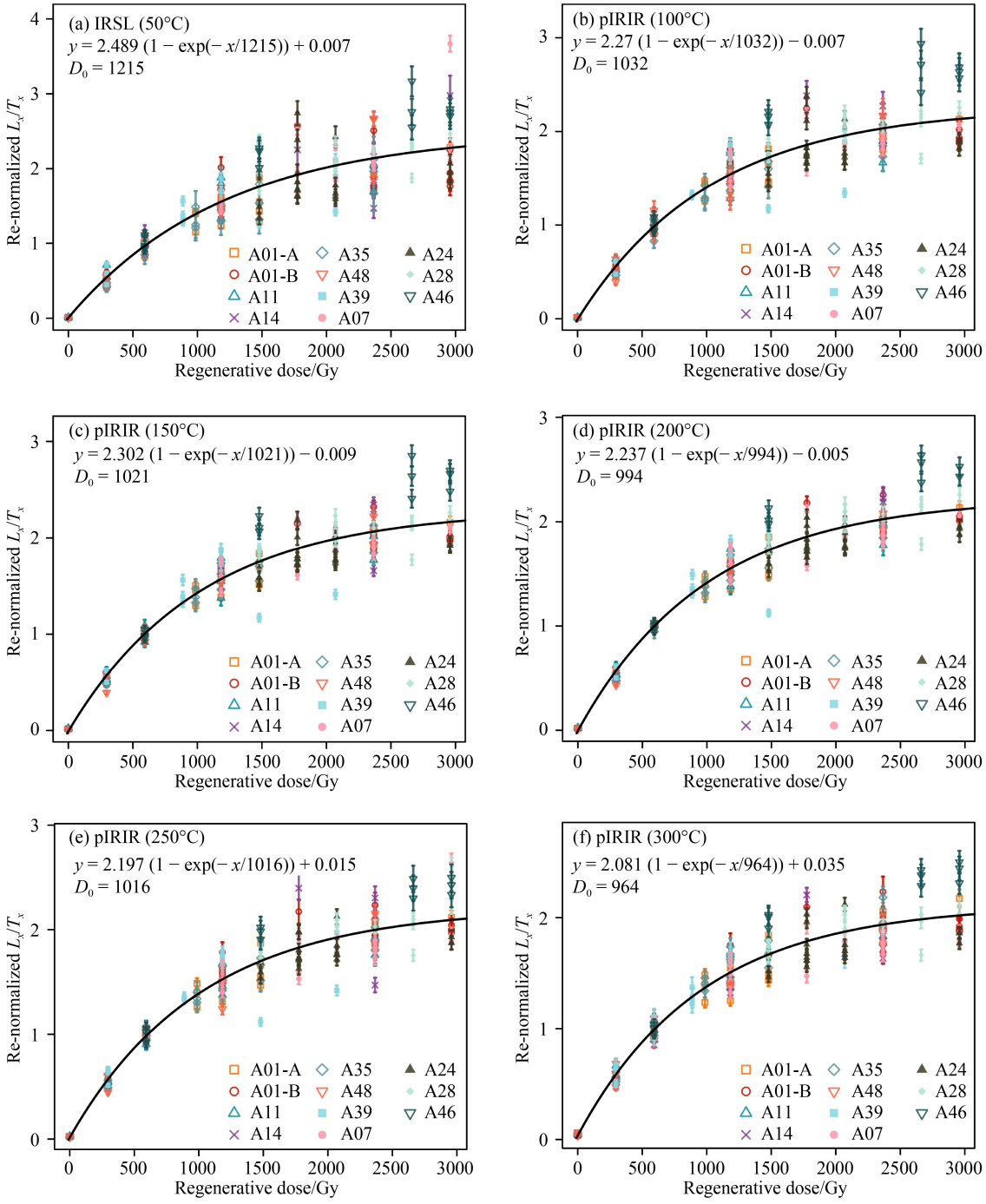

Fig. 4 Establishment of the SGC with the 'MAR with heat' protocol based on 11 K-feldspar samples. The renormalization dose was ~600 Gy. The renormalized L_x/T_x shown in (a)–(f) are for IR stimulation temperatures of 50°C, 100°C, 150°C, 200°C, 250°C, and 300°C, respectively. The renormalized L_x/T_x data were fitted using a single saturating exponential (SSE) function: $y = y_0 + A^*(1–\exp(–x/D_0))$.

fitted by using a single saturating exponential function (Fig. 4). For example, the MAR SGC of the MET-pIRIR$_{300}$ signal can be well fitted using the function $y = 0.041 + 4.682\times(1-\exp(-x/989))$, where y is the renormalized L_x/T_x and x is the dose. The D_0 value of the MET-pIRIR$_{300}$ signal is 989 Gy. The MAR SGC of the IRSL and MET-pIRIR signals at 50°C, 100°C, 150°C, 200°C, 250°C, and 300°C are shown in Fig. 4.

The established MAR SGC was used to determine the D_e values. The natural signal (L_n/T_n) and the signal of a regenerative dose (L_r/T_r) were measured. Aliquots of the latter were bleached for 8 h before being given regenerative doses that closely approximated the expected D_e values. The median values (L_r/T_r) were used to renormalize the L_n/T_n values. The renormalized L_n/T_n values were then projected onto the MAR SGC to estimate the D_e values using the following equation:

$$f(D_e) = f(D_r)\frac{L_n/T_n}{L_x/T_x}, \quad (1)$$

where $f(D_e)$ and $f(D_r)$ are the corresponding functional values of D_e and D_r in the MAR SGC.

For the dose recovery test, heating the sample to 500°C (Table 1) in the MAR protocol removed the influence of the pre-dose, and the test dose signals were used only for normalization between aliquots. The test dose size had no impact on the MAR D_e estimation (Zhang et al. 2021, Zhang et al. 2022). Therefore, no dose recovery tests were conducted for the MAR protocol study, as suggested by Zhang et al. (2022).

2.4.3 Residual dose measurements

The residual dose caused by the unbleachable component of the MET-pIRIR signals may influence the final D_e results. Three samples (A01-A, 24, and 35) were selected to determine the residual doses. Three groups of two aliquots for each sample were solar bleached for 2, 4, and 8 h and then measured using the MET-pIRIR procedure. The obtained D_e values are plotted against bleaching time and stimulation temperature (Fig. 5).

2.4.4 Fading test

To assess the possibility of anomalous fading for the MET-pIRIR signals of the old samples, eight samples were selected. Nine aliquots from each sample were measured using a single-aliquot fading test procedure similar to that described by Auclair et al. (2003) but based on the MET-pIRIR procedure (Table 1). Each aliquot was given a dose of 1000 Gy and then preheated and stored for periods of up to approximately two months in the dark at room temperature.

2.4.5 Environmental dose rate

The concentrations of these radioactive elements were obtained using an inductively coupled plasma mass spectrometry (ICP–MS) instrument for U and Th and an inductively coupled plasma optical emission spectroscopy (ICP–OES) instrument for K. The internal K and Rb concentrations of K-feldspar were assumed to be 13 ± 1% and 400 ± 100 ppm, respectively (Huntley and Baril 1997, Zhao and Li 2005). The contribution of cosmic rays to the dose rate was estimated for each sample as a function of the density of cover deposits, depth, altitude, and geomagnetic latitude (Prescott and Hutton 1994). However, the contribution of cosmic rays to the dose rate can be considered negligible when the depth of the overlying sediments is greater than ~30 m.

Estimating the water content in the sediments remains challenging, as the compression caused by increasing overlying sediment deposition can lead to changes in the water content over the burial history, particularly in the organic layer. However, for incompressible materials, such as sand and silt, measurements of the water content in the laboratory indicate limited changes (Roberts et al., 2021). In this study, we used the current water content as a reference for the average long-term water content. An error of 10% was applied to account for any likely variations over the burial history.

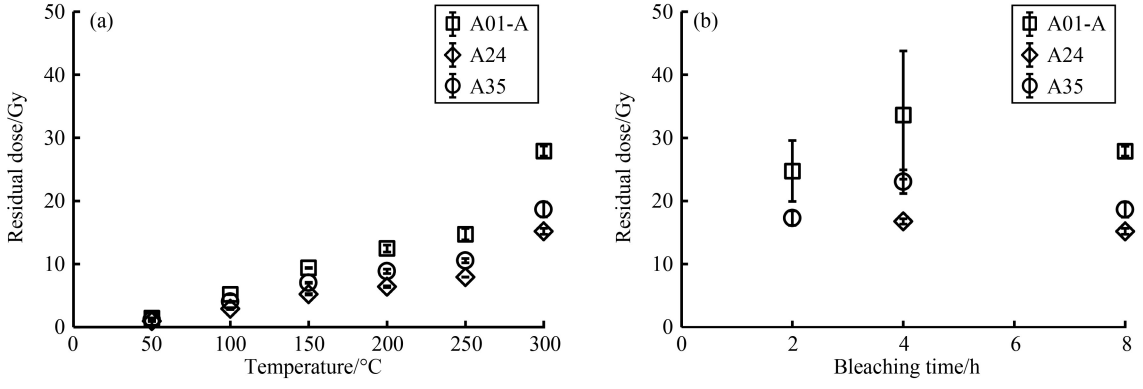

Fig. 5 Residual dose test for three samples. (a) Residual doses after eight hours of solar bleaching for different IRSL and MET-pIRIR signals. (b) Residual doses of MET-pIRIR$_{300}$ signals after two, four, and eight hours of solar bleaching.

3 Results and discussion

3.1 Radiocarbon ages

The results of radiocarbon dating are presented in Table 2. All five radiocarbon ages are older than 43.5 ka BP, which is considered beyond the upper limit of radiocarbon dating.

3.2 K-feldspar pIRIR ages

3.2.1 Characteristics of the IRSL and pIRIR signals

Figure 5 shows the residual doses of the MET-pIRIR$_{300}$ signals of three representative samples (A01-A, 24, and 35). The results indicate that the residual doses reached an unbleachable level after two hours of solar bleaching, with values ranging from 17 Gy to 25 Gy. Because the residual dose is negligible compared to the large natural D_e value (> 1200 Gy), no residual dose was subtracted in this study.

Figure 6 shows the g values (t_c normalized to 2 days) for the MET-pIRIR$_{300}$ signals for eight samples. The g values are consistently zero (−0.9%–3.4%/decade) within the uncertainty ranges, even for the samples collected near the bottom of the borehole. The g values decrease as the stimulation temperature increases (Fig. S1). The results suggest that the MET-pIRIR procedure can isolate less-fading or nonfading signals from our samples (Li and Li, 2011).

The pIRIR$_{300}$ D_e distributions are shown in Figs. 7 and S2. The overdispersion (OD) value is applied to describe the D_e distribution. The majority of samples (18 out of 24) have OD values less than 20% (Figs. 7 and S2), indicating that the D_e values are mainly centered on the average value (Galbraith and Roberts, 2012). The characteristic dose (D_0) of the pIRIR$_{300}$ signal is ~964 Gy. In conjunction with the stratigraphic order, the pIRIR$_{300}$ signals appear to be saturated for samples collected at depths below ~37 m (sample A18) if the upper dating limit is defined by $2D_0$ for single-saturating exponential growth (Wintle and Murray, 2006). Therefore, the larger OD values of the saturated samples (Fig. S2) are still acceptable, and the final D_e value was calculated using the central age model (CAM). For the saturated samples, the calculated D_e values should be regarded only as the minimum D_e values.

3.2.2 D_e vs. temperature (D_e-T) plots

The D_e-T plots demonstrate an increasing trend with increasing stimulation temperature (Fig. 8), as smaller fading rates of pIRIR signals occur at higher temperatures. Some samples (e.g., A01-A, A01-B, A05, and A07) show consistent D_e values for pIRIR signals at higher stimulated temperatures, indicating the presence of a D_e-T plateau (Fig. 8). This suggests that these high-temperature signals are less affected by anomalous fading and that no fading correction is needed.

In contrast, for some samples (e.g., A18, A25, A35, A44, and A46), the D_e values increase from 250°C to 300°C (Figs. S3 and S4), making it difficult to determine whether the pIRIR$_{300}$ signals are sufficiently stable. However, the g values indicate negligible fading of the pIRIR$_{300}$ signals (Fig. 6). On the other hand, the pIRIR$_{300}$ signals appear to be saturated for samples collected at deeper locations (e.g., sample A44), which likely explains the absence of a D_e-T plateau.

3.2.3 Reliability of ages and implications for the timing of impact events

Two near-surface replicate samples, i.e., A01-A and A01-B, yield luminescence ages of 331 ± 30 and 334 ± 30 ka, respectively (Table 3), which are significantly older than the radiocarbon ages. Considering the upper limit of radiocarbon dating, the radiocarbon ages would be underestimated. However, the MAR MET-pIRIR method using K-feldspar extends the upper limit of luminescence dating to approximately 350 ka and even up to 780 ka for dating loess-paleosol sequences on the Loess Plateau (Chen et al. 2015; Rui et al. 2020; Zhang et al. 2022). This suggests the reliability of the dating results for samples A01-A and A01-B.

The pIRIR$_{300}$ ages increase from sample A01-A (331 ± 30 ka) to sample A18 (570 ± 43 ka) within the age range (Fig. 9 and Table 3). However, there are two unexpected older ages for samples A05 (727 ± 57 ka) and A16 (737 ± 57 ka). For sample A05, which was obtained from the organic peat layer (Fig. 1(c)), the dose rate (1.77 ± 0.10 Gy/ka) is significantly lower than the average values of the other

Table 2 AMS ^{14}C dating results for the five samples. The radiocarbon ages were calibrated by BetaCal4.20 and IntCal20 (Reimer et al., 2020). The ages are expressed in years before present (BP), where 'present' is defined as 1950 AD.

Sample ID	Depth/m	Materials	Conventional ^{14}C age (a BP)	Calibrated ^{14}C age (cal a BP)
B05-70	6.26	Plant	> 43500 BP	Older than cal BC 44650 (cal BP 46600)
B06-78	8.60	Plant	> 43500 BP	Older than cal BC 44650 (cal BP 46600)
B06-200	9.82	Plant	> 43500 BP	Older than cal BC 44650 (cal BP 46600)
B06-144	9.26	Plant	> 43500 BP	Older than cal BC 44650 (cal BP 46600)
B10-77	14.50	Plant	> 43500 BP	Older than cal BC 44650 (cal BP 46600)

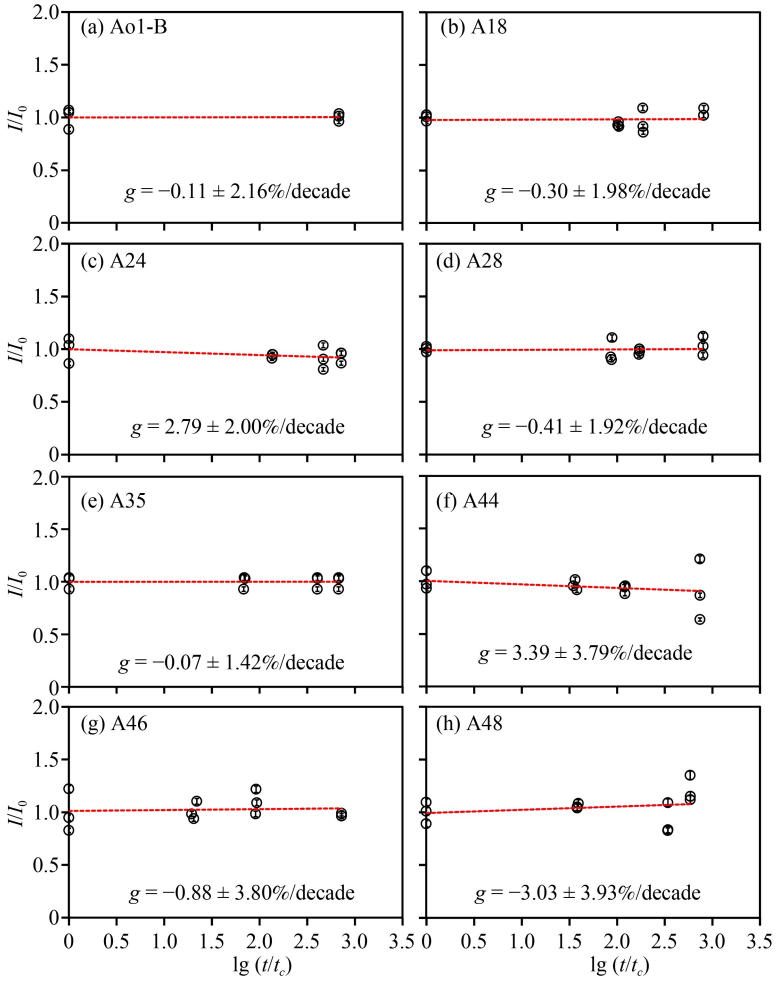

Fig. 6 Fading rate measurements of the MET-pIRIR$_{300}$ signals of eight samples. The t_c is 1.96 h.

silty and sandy samples (3–5 Gy/ka) (Fig. 9 and Table 3). Similarly, the dose rate of sample A16 (2.72 ± 0.17 Gy/ka) is lower than the mean dose rate (Fig. 9). On the other hand, sample A22 consists of siderite layers, yielding lower U, Th, and K contents; therefore, the dose rate of sample A22 is also markedly lower than that of the other samples (Fig. 9). Therefore, the much lower dose rates related to the different sedimentary conditions are the main reasons for the extremely old age results. Based on the pIRIR$_{300}$ ages of samples with depths up to ~37 m, the mean sedimentation rate is approximately 0.111 ± 0.018 mm/year.

The measured pIRIR$_{300}$ ages of the samples collected at depths below ~37 m and their D_e values are larger than those in the $2D_0$ range, and the ages are relatively scattered within the range of 374–1149 ka (Table 3), which may exceed the upper dating limit for K-feldspar pIRIR signals. However, in practice, defining this upper limit of reliability can be difficult because it varies according to the specific luminescence signal used, the dose rate, and individual samples. Considering the saturation dose of the pIRIR$_{300}$ signal ($2D_0$, ~1928 Gy) and stratigraphic order, the pIRIR$_{300}$ signals saturate in samples collected at depths below ~37 m (sample A18). Given the same sedimentation rate based on the upper luminescence ages (0.111 ± 0.018 mm/year), it is suggested that the Xiuyan impact event occurred at ~1201 ± 133 ka.

3.3 Evolution of the Xiuyan impact crater lake

Based on the geochronological, sedimentological, and geomorphological investigations, we then established the evolution of the Xiuyan impact crater lake. First, an ~55 m-diameter aero siderite or ~115 m-diameter aerolite (Wang et al., 2013) struck the Earth at ~1201 ± 133 ka and created the ~1800 m-diameter Xiuyan impact crater in the Liaodong Peninsula in northeast China (Fig. 10(a)). In the impact crater, a lake eventually formed under the influence of groundwater flow and precipitation (Fig. 10(b)). In the initial stage, the lake was shallow, and the hydrological conditions were unstable, which was revealed by the disordered silt laminations with white and dark sand layers from ~105–100 m (Fig. 2). As more water accumulated, the Xiuyan impact crater lake became deeper (Fig. 10(c)). In this stage (~100–23 m), the deposited lake sediments are characterized by gray silty

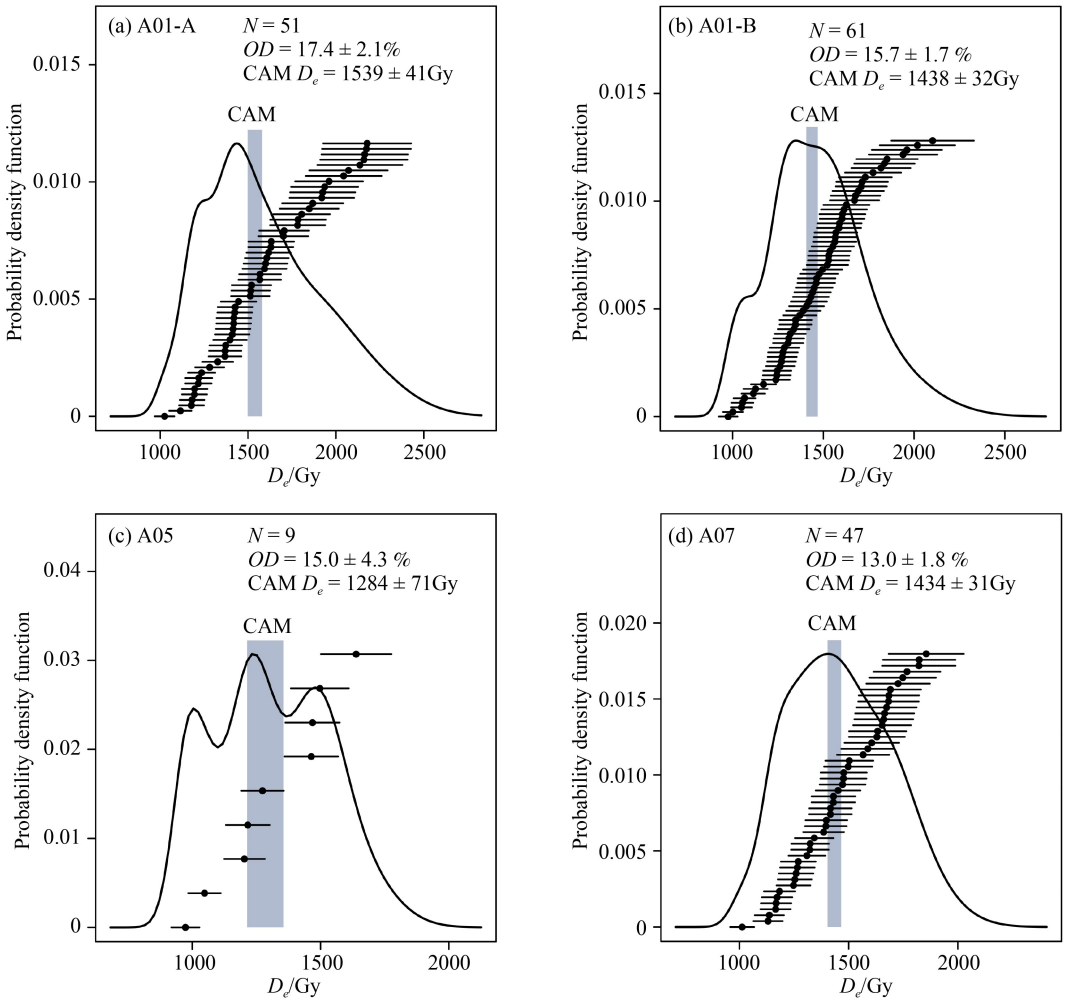

Fig. 7 Distribution of D_e values of MET-pIRIR$_{300}$ signals for four unsaturated samples. N represents the number of aliquots for the SGC D_e calculation.

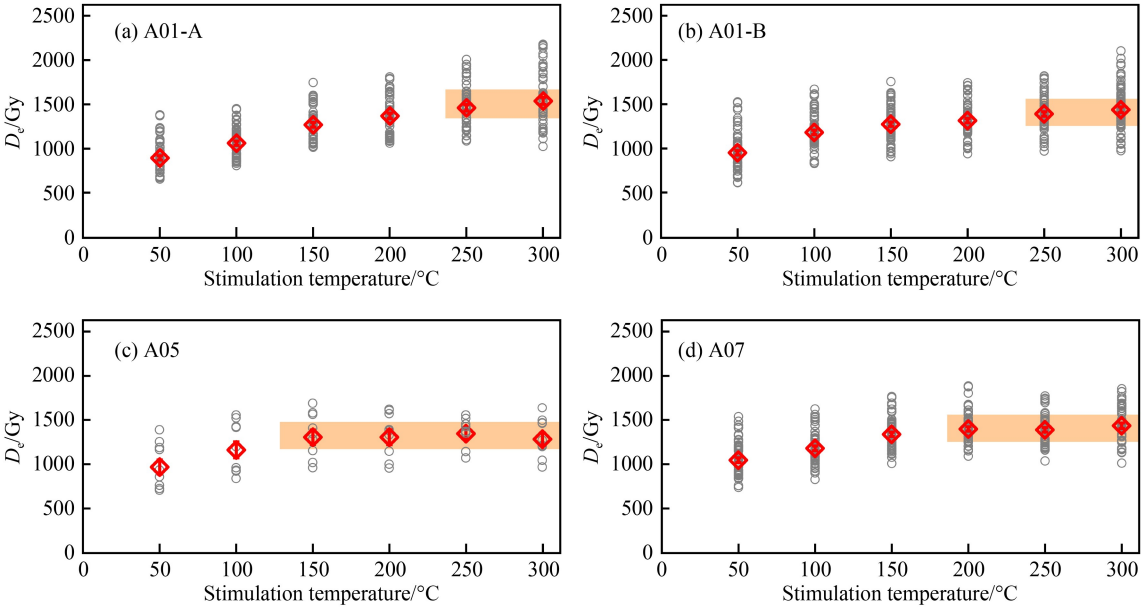

Fig. 8 D_e values plotted against different IR stimulation temperatures with the MET-pIRIR protocol for four unsaturated samples. Red diamonds indicate the average D_e values.

Table 3 Sample depths, dosimetry data, MET-pIRIR$_{300}$ D_e values, MET-pIRIR$_{300}$ ages, and associated errors (1σ) for all samples.

Sample ID	Depth/m[1]	Grain size/μm	U/ppm	Th/ppm	K/%	Water content/%	Dose rate Gy/ka[2]	Number of aliquots	D_e/Gy	Age/ka[3]
A01-A	1.7	90-125	3.22 ± 0.31	14.12 ± 1.34	2.64 ± 0.25	5 ± 10	4.66 ± 0.40	51	1539 ± 41	331 ± 30
A01-B	1.8	90-125	2.85 ± 0.27	15.14 ± 1.44	2.20 ± 0.21	3 ± 10	4.31 ± 0.37	61	1438 ± 32	334 ± 30
A05	9.8	63-90	2.80 ± 0.27	13.62 ± 1.29	1.57 ± 0.15	103 ± 10	1.77 ± 0.10	9	1284 ± 71	727 ± 57
A07	14.8	90-125	4.36 ± 0.41	15.59 ± 1.48	2.47 ± 0.23	55 ± 10	3.18 ± 0.20	47	1434 ± 31	451 ± 30
A09	19.4	63-90	4.91 ± 0.47	14.82 ± 1.41	2.49 ± 0.28	41 ± 10	3.46 ± 0.26	21	1986 ± 72	574 ± 47
A11	24.5	63-90	3.81 ± 0.36	16.55 ± 1.57	2.53 ± 0.24	53 ± 10	3.12 ± 0.21	48	1484 ± 46	476 ± 35
A14	30.7	63-90	3.72 ± 0.35	16.66 ± 1.58	2.68 ± 0.25	50 ± 10	3.26 ± 0.22	33	1918 ± 107	588 ± 52
A16	33.0	63-90	4.29 ± 0.41	18.03 ± 1.71	2.19 ± 0.21	70 ± 10	2.72 ± 0.17	23	2008 ± 94	737 ± 57
A18	37.0	90-125	3.30 ± 0.31	15.97 ± 1.52	2.16 ± 0.21	38 ± 10	3.17 ± 0.22	28	1808 ± 51	570 ± 43
A22	42.5	63-90	1.87 ± 0.18	9.83 ± 0.93	1.28 ± 0.12	52 ± 10	1.76 ± 0.12	26	2024 ± 115	1149 ± 100
A23	45.1	63-90	3.23 ± 0.31	16.47 ± 1.56	2.44 ± 0.28	56 ± 10	2.89 ± 0.21	26	2161 ± 61	747 ± 57
A24	47.3	90-125	3.13 ± 0.30	16.41 ± 1.56	2.54 ± 0.24	37 ± 10	3.43 ± 0.24	39	1646 ± 59	480 ± 38
A25	50.1	63-90	2.83 ± 0.27	13.83 ± 1.31	2.39 ± 0.27	40 ± 10	3.01 ± 0.23	23	2435 ± 121	808 ± 74
A26	51.9	63-90	3.40 ± 0.32	16.03 ± 1.52	2.57 ± 0.24	41 ± 10	3.29 ± 0.23	21	2184 ± 81	664 ± 53
A28	55.5	90-125	3.25 ± 0.31	15.63 ± 1.48	2.48 ± 0.24	32 ± 10	3.51 ± 0.26	26	1594 ± 62	454 ± 38
A31	61.3	90-125	3.69 ± 0.35	17.33 ± 1.65	2.60 ± 0.25	38 ± 10	3.58 ± 0.25	28	1859 ± 50	519 ± 39
A33	66.3	63-90	3.64 ± 0.35	17.56 ± 1.67	2.22 ± 0.21	42 ± 10	3.15 ± 0.22	24	1973 ± 84	626 ± 51
A35	71.6	90-150	3.41 ± 0.32	18.08 ± 1.72	2.26 ± 0.22	49 ± 10	3.12 ± 0.22	39	1596 ± 60	511 ± 41
A37	76.8	90-125	3.68 ± 0.35	17.66 ± 1.68	2.53 ± 0.24	34 ± 10	3.66 ± 0.26	20	2047 ± 74	559 ± 45
A39	82.0	90-150	2.90 ± 0.28	12.95 ± 1.23	1.88 ± 0.18	32 ± 10	2.90 ± 0.22	13	2329 ± 145	802 ± 79
A42	87.6	90-125	3.96 ± 0.38	17.84 ± 1.70	2.54 ± 0.24	42 ± 10	3.49 ± 0.24	22	1337 ± 150	383 ± 50
A44	91.1	90-150	4.17 ± 0.40	16.69 ± 1.59	2.64 ± 0.25	37 ± 10	3.71 ± 0.27	30	2072 ± 80	559 ± 46
A46	96.1	90-150	5.09 ± 0.48	17.13 ± 1.63	2.72 ± 0.26	35 ± 10	4.01 ± 0.30	41	1787 ± 61	445 ± 36
A48	99.1	90-125	4.48 ± 0.43	8.59 ± 0.82	1.60 ± 0.15	11 ± 10	3.24 ± 0.26	70	1212 ± 49	374 ± 34

Notes: [1] Depth below the core top.[2] Assuming internal K and Rb concentrations of 13 ± 1% and 400 ± 100 ppm, respectively.[3] Empirically, the upper dating limit is defined by $2D_0$ for single-saturating exponential growth, and the saturation dose of the MET-pIRIR$_{300}$ signal is ~1928 Gy. Considering the stratigraphic order, the K-feldspar pIRIR$_{300}$ signals saturate for samples below ~14.8 m depth.

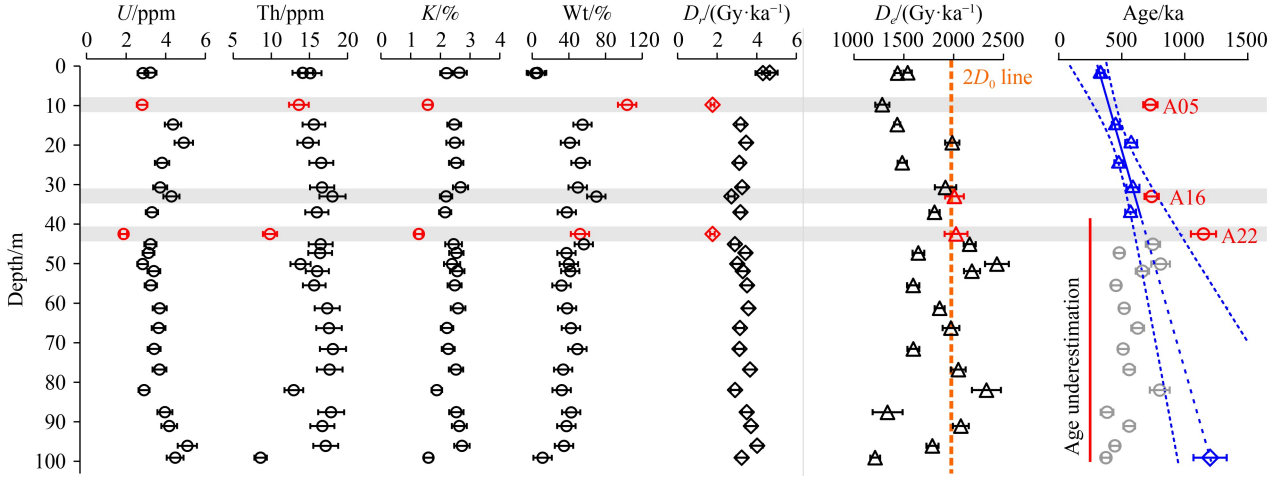

Fig. 9 Sample depths; concentrations of U, Th, and K; MET-pIRIR$_{300}$ D_e values; and MET-pIRIR$_{300}$ ages for all samples. The $2D_0$ value (empirical upper dating limit) is ~1928 Gy. The ages start to be underestimated for samples collected below ~37 m in the core. The gray bars indicate three samples with anomalous concentrations of U, Th, and K; dose rates; and dating ages compared to the average values. In the age-depth model, blue triangles are the ages (above a depth of 37 m in the core) used for modeling, while gray and red circles are ages not used for modeling. The blue diamond indicates the modeling result of 1201 ± 133 ka.

clays, occasional thin dark sand layers, and gray siderite and oligonite-rich interlayers (Fig. 2). In addition, submillimeter- to millimeter-scale laminations are universal but discontinuous within this interval of ~100–23 m, and the total organic carbon content is lower than 5%, which is similar to that of volcanic lakes during glacial periods (Liu et al., 2010, 2015). When the lake level increased to a level beyond that of the crater rim, overflow naturally occurred via the north-eastern breach (Figs. 1(c) and 10(d)). Subsequently, the lake became shallower, as indicated by the disappearance of the submillimeter- to millimeter-scale laminations, and the TOC contents increased from ~23.0 m to ~11.9 m (Fig. 2). The lake then turned into a peat bog, characterized by abundant wood fragments and organic detritus (TOC contents of ~5%–20%) from ~11.9 m to ~8.5 m (Fig. 2). Afterward, alluvial deposits, which consisted of steel gray and grayish-white sandy silt with gravels (Fig. 2), were deposited in the crater until it was filled with sediments (Fig. 10(d)).

4 Conclusions

In this study, we present further geochronological constraints on the formation of the Xiuyan impact crater in northeast China by determining the ages of lake sediments using luminescence and radiocarbon dating methods. The results show that all the radiocarbon ages of the lake sediments exceed the upper dating limit, and the luminescence ages saturate below a depth of ~37 m. The results of the age-depth model show that the Xiuyan impact event occurred at approximately 1201 ± 133 ka, which is much older than the previously reported limited AMS radiocarbon age of ~50 ka BP. By incorporating sedimentological, geomorphological, and geochronological analyses, the evolutionary history of the Xiuyan impact crater lake was reconstructed. We propose that the crater lake underwent the stages of initial formation, subsequent filling with water and sediment, overflow, and eventual disappearance at ~331-334 ka. Further geochronological investigations are needed to precisely constrain the timing of the impact event.

Acknowledgments We thank Mr. Chunxin Wang from the University of Science and Technology of China for his assistance in analyzing the luminescence data. We acknowledge the use of refrigeratory facility at the Beijing National Observatory of Space Environment, Institute of Geology and Geophysics, Chinese Academy of Sciences. This work was supported by the National Natural Science Foundation of China (Grant Nos. 41972190, 42302344).

Author contributions Zeyang Zhu and Jiaqi Liu organized the research. Zeyang Zhu, Jing Wu, Yawei Li, Zhihao Sun, Bin Zhang, and Jiaqi Liu investigated and collected the samples. Zeyang Zhu, Chang Huang, and Sheng-Hua Li designed and performed the experiments and conceptualized the results. Chang Huang analyzed the data. Zeyang Zhu and Chang Huang wrote the paper. Jiaqi Liu and Sheng-Hua Li reviewed the paper. All authors contributed to the discussion.

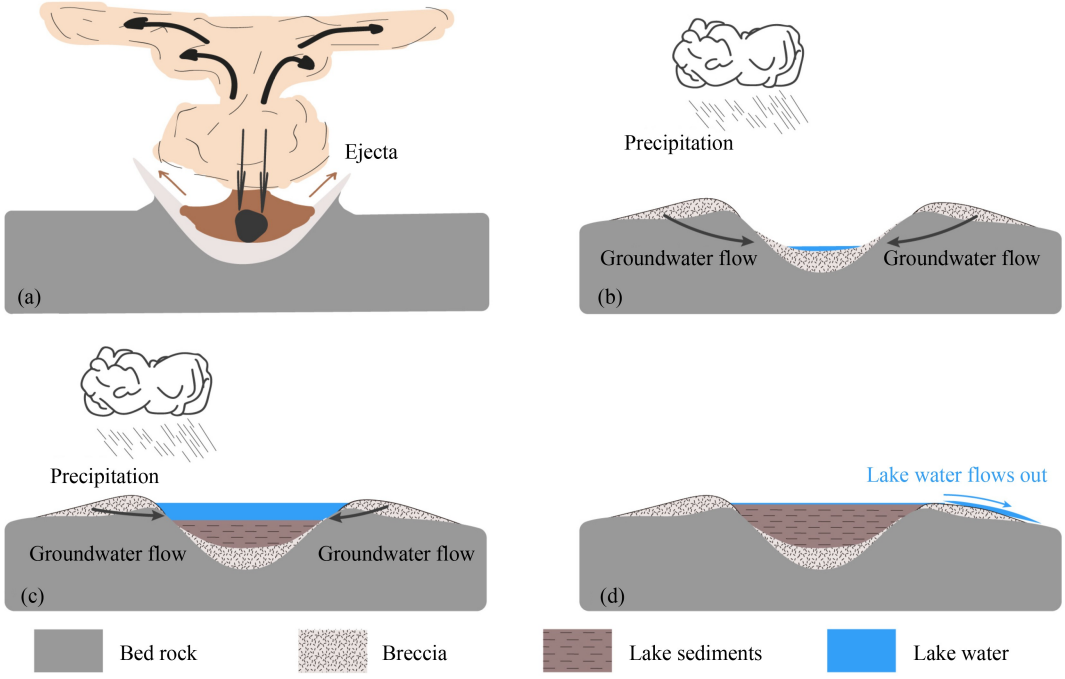

Fig. 10 Sketch showing the evolution of Xiuyan crater lake. (a) The crater was created by a terrestrial impact. (b) Water and surrounding materials rapidly filled the crater, forming a crater lake. (c) The crater lake was filled mainly with water and partially with lake sediments characterized by gray silty clays and submillimeter- to millimeter-scale laminations under deep-water conditions. (d) As the lake level increased to a level beyond that of the crater rim, overflow naturally occurred. Eventually, when the crater became filled with sediments, no further materials were deposited.

Supplementary material is available in the online version of this article at http://dx.doi.org/10.1007/s11707-024-1133-y and is accessible for authorized users.

Conflict of interest The authors declare that they have no conflicts of interest.

References

Auclair M, Lamothe M, Huot S (2003). Measurement of anomalous fading for feldspar IRSL using SAR. Radiat Meas, 37(4−5): 487–492

Chen M, Xiao W, Xie X, Tan D, Cao Y (2009) Xiuyan crater, China: impact origin confirmed. Chinese Sci Bull 54, 3507–3511 (in Chinese)

Bøtter-Jensen L, Thomsen K J, Jain M, (2010). Review of optically stimulated luminescence (OSL) instrumental developments for retrospective dosimetry. Radia Meas, 45(3−6): 253–257

Chen Y, Li S H, Li B, Hao Q, Sun J (2015). Maximum age limitation in luminescence dating of Chinese loess using the multiple-aliquot MET-pIRIR signals from K-feldspar. Quat Geochronol, 30: 207–212

Firestone R B, West A, Kennett J P, Becker L, Bunch T E, Revay Z S, Schultz P H, Belgya T, Kennett D J, Erlandson J M, Dickenson O J, Goodyear A C, Harris R S, Howard G A, Kloosterman J B, Lechler P, Mayewski P A, Montgomery J, Poreda R, Darrah T, Hee S S Q, Smith A R, Stich A, Topping W, Wittke J H, Wolbach W S (2007). Evidence for an extraterrestrial impact 12, 900 years ago that contributed to the megafaunal extinctions and the Younger Dryas cooling. Proc Natl Acad Sci USA, 104(41): 16016–16021

Galbraith R F, Roberts R G (2012). Statistical aspects of equivalent dose and error calculation and display in OSL dating: An overview and some recommendations. Quat Geochronol, 11: 1–27

Grieve R A F, Pesonen L J (1992). The terrestrial impact cratering record. Tectonophysics, 216(1−2): 1–30

Huntley D J, Baril M (1997). The K content of the K-feldspars being measured in optical dating or in thermoluminescence dating. Anc TL, 15: 11–13

Jacobs Z, Li B, Karkanas P, Tourloukis V, Thompson N, Panagopoulou E, Harvati K (2018). Optical dating of K-feldspar grains from Middle Pleistocene lacustrine sediment at Marathousa 1 (Greece). Quat Int, 497: 170–177

Jourdan F, Reimold W U, Deutsch A (2012). Dating terrestrial impact structures. Elements (Quebec), 8(1): 49–53

Li B, Jacobs Z, Roberts R G (2017). An improved multiple-aliquot regenerative-dose (MAR) procedure for post-IR IRSL dating of K-feldspar. Anc TL, 35: 1–10

Li B, Jacobs Z, Roberts R G, Li S H (2013). Extending the age limit of luminescence dating using the dose-dependent sensitivity of MET-pIRIR signals from K-feldspar. Quat Geochronol, 17: 55–67

Li B, Li S H (2012). Luminescence dating of Chinese loess beyond 130 ka using the non-fading signal from K-feldspar. Quat Geochronol, 10: 24–31

Li B, Li S H (2011). Luminescence dating of K-feldspar from sediments: A protocol without anomalous fading correction. Quat Geochronol, 6(5): 468–479

Liu J L, Liu Q, Chu G, Wu J, Liu J Q (2015) Sediment record at lake sifanshan in the central-northern part of the Great Xing'an Range, northeast China since 15.4 ka B.P. Quart Sci 35, 901–912 (in Chinese)

Liu K X, Chen M, Ding X F, Fu D P, Ding P, Shen C D, Xiao W S (2013). AMS radiocarbon dating of lacustrine sediment from an impact crater in northeastern China. Nucl Instrum Methods Phys Res B, 294: 593–596

Liu Q, Li Q, Wang L, Chu G (2010). Stable carbon isotope record of bulk organic matter from a sediment core at moon lake in the middle part of the Daxing'an Mountain range, northeast China during the last 21 ka. Quart Sci, 30: 1069–1077 (in Chinese)

Prescott J R, Hutton J T (1994). Cosmic ray contributions to dose rates for luminescence and ESR dating: large depths and long-term time variations. Radiat Meas, 23(2−3): 497–500

Ramsey, C.B. (2009) Bayesian analysis of radiocarbon dates. Radiocarbon 51: 337–360

Reimer P J, Austin W E N, Bard E, Bayliss A, Blackwell P G, Bronk Ramsey C, Butzin M, Cheng H, Edwards R L, Friedrich M, Grootes P M, Guilderson T P, Hajdas I, Heaton T J, Hogg A G, Hughen K A, Kromer B, Manning S W, Muscheler R, Palmer J G, Pearson C, van der Plicht J, Reimer R W, Richards D A, Scott E M, Southon J R, Turney C S M, Wacker L, Adolphi F, Büntgen U, Capano M, Fahrni S M, Fogtmann-Schulz A, Friedrich R, Köhler P, Kudsk S, Miyake F, Olsen J, Reinig F, Sakamoto M, Sookdeo A, Talamo S (2020). The IntCal20 Northern Hemisphere radiocarbon age calibration curve (0–55 cal kBP). Radiocarbon, 62(4): 725–757

Roberts H M, Ramsey C B, Chapot M S, Deino A L, Lane C S, Foerster V, Lamb H F, Scha F, Viehberg F A (2021). Using multiple chronometers to establish a long, directly-dated lacustrine record: Constraining >600000 years of environmental change at Chew Bahir, Ethiopia. Quat Sci Rev, 266: 107025

Rui X, Li B, Guo Y (2020). Testing the upper limit of luminescence dating based on standardised growth curves for MET-pIRIR signals of K-feldspar grains from northern China. Quat Geochronol, 57: 101063

Schmieder M, Kring D A (2020). Earth's impact events through geologic time: a list of recommended ages for terrestrial impact structures and deposits. Astrobiology, 20(1): 91–141

Schulte P, Alegret L, Arenillas I, Arz J A, Barton P J, Bown P R, Bralower T J, Christeson G L, Claeys P, Cockell C S, Collins G S, Deutsch A, Goldin T J, Goto K, Grajales-Nishimura J M, Grieve R A F, Gulick S P S, Johnson K R, Kiessling W, Koeberl C, Kring D A, MacLeod K G, Matsui T, Melosh J, Montanari A, Morgan J V, Neal C R, Nichols D J, Norris R D, Pierazzo E, Ravizza G, Rebolledo-Vieyra M, Reimold W U, Robin E, Salge T, Speijer R P, Sweet A R, Urrutia-Fucugauchi J, Vajda V, Whalen M T, Willumsen P S (2010). The chicxulub asteroid impact and mass extinction at the Cretaceous-Paleogene boundary. Science, 327(5970): 1214–1218

Sweatman M B (2021). The Younger Dryas impact hypothesis: review of the impact evidence. Earth Sci Rev, 218: 103677

Wang X., Luo L, Guo H, Mu L, Li C, Ji W, Cai H (2013) Cratering process and morphological features of the Xiuyan impact crater in

northeast China. Sci China Earth Sci 56: 1629–1638 (in Chinese)

Wintle A G, Murray A S (2006). A review of quartz optically stimulated luminescence characteristics and their relevance in single-aliquot regeneration dating protocols. Radiat Meas, 41(4): 369–391

Zhang J, Hao Q, Li S H (2022). An absolutely dated record of climate change over the last three glacial–interglacial cycles from Chinese loess deposits. Geology, 50(10): 1116–1120

Zhang J, Li S H, Wang X, Hao Q, Hu G, Chen Y (2021). Comparison of equivalent doses obtained with various post-IR IRSL dating protocols of K-feldspar. Geochronometria, 1695(1): 129–137

Zhao H, Li S H (2005). Internal dose rate to K-feldspar grains from radioactive elements other than potassium. Radiat Meas, 40(1): 84–93